


First-principles study on magneto-optical effects in the ferromagnetic semiconductors $\text{Y}_3\text{Fe}_5\text{O}_{12}$ and $\text{Bi}_3\text{Fe}_5\text{O}_{12}$

Wei-Kuo Li¹ and Guang-Yu Guo^{1,2,*}¹*Department of Physics and Center for Theoretical Physics, National Taiwan University, Taipei 10617, Taiwan*²*Physics Division, National Center for Theoretical Sciences, Taipei 10617, Taiwan*
 (Received 2 August 2020; revised 6 January 2021; accepted 8 January 2021; published 25 January 2021)

The magneto-optical (MO) effects are a powerful probe of magnetism and electronic structure of magnetic solids but also have valuable applications in high-density data-storage technology. Yttrium iron garnet ($\text{Y}_3\text{Fe}_5\text{O}_{12}$) (YIG) and bismuth iron garnet ($\text{Bi}_3\text{Fe}_5\text{O}_{12}$) (BIG) are two widely used magnetic semiconductors with significant magneto-optical effects. In this paper, we present a thorough theoretical investigation on magnetism, electronic, optical, and MO properties of YIG and BIG, based on the density functional theory with the generalized gradient approximation plus on-site Coulomb repulsion. We find that YIG exhibits significant MO Kerr and Faraday effects in UV frequency range that are comparable to ferromagnetic iron. Moreover, BIG shows gigantic MO effects in visible frequency region that are several times larger than YIG. This is because the calculated MO conductivity (σ_{xy}) of BIG is nearly ten times larger than that of YIG. Interestingly, the calculated band structures reveal that BIG is a single spin semiconductor. They also show that in YIG, Y *sd* orbitals mix mainly with the high-lying conduction bands, leaving Fe *d* orbital dominated lower conduction bands almost unaffected by the spin-orbit coupling (SOC) on the Y atom. In contrast, Bi *p* orbitals in BIG hybridize significantly with Fe *d* orbitals in the lower conduction bands, leading to large SOC-induced band splitting in the bands. Consequently, the MO transitions between the upper valence bands and lower conduction bands are greatly enhanced when Y is replaced by heavier Bi. Our calculated Kerr and Faraday rotation angles of YIG as well as Faraday rotation angles for BIG agree well with the available experimental values. Thus, we believe that our predicted giant MO Kerr effect in BIG will stimulate further MOKE experiments on high-quality BIG crystals. This work thus shows that the iron garnets not only offer a useful platform for exploring the interplay of spin current, magnetism, and optics degrees of freedom, but also have promising applications in high-density MO data-storage and low-power consumption spintronic nanodevices.

DOI: [10.1103/PhysRevB.103.014439](https://doi.org/10.1103/PhysRevB.103.014439)

I. INTRODUCTION

Yttrium iron garnet ($\text{Y}_3\text{Fe}_5\text{O}_{12}$, YIG) is a ferrimagnetic semiconductor with excellent magnetic properties such as high Curie temperature T_c [1], low Gilbert damping $\alpha \sim 6.7 \times 10^{-5}$ [2–4], and long spin wave propagating length [5]. Various applications such as spin pumping require a nonmetallic magnet. YIG is thus routinely used for spin pumping purposes [4]. It is also widely used as a magnetic insulating substrate for purposes such as introducing magnetic proximity effect while avoiding electrical shortcut [6]. YIG has high Curie temperature, which is good for applications across a wide temperature range. The low Gilbert damping of YIG also makes it a good microwave material. YIG thus becomes a famous material in the field of spintronics, where coupling between magnetism, microwave, and spin current becomes possible.

Magneto-optical (MO) effects are important examples of light-matter interactions in magnetic phases [7,8]. When a linearly polarized light beam is shined onto a magnetic material, the reflected and transmitted light becomes elliptically polarized. The principal axis is rotated with respect to the

polarization direction of incident light beam. The former and latter effects are termed MO Kerr (MOKE) and MO Faraday (MOFE) effects, respectively. MOKE allows us to detect the magnetization locally with a high spatial and temporal resolution in a noninvasive fashion. Furthermore, magnetic materials with large MOKE would find valuable MO storage and sensor applications [9,10]. Thus it has been widely used to probe the electronic and magnetic properties of solids, surface, thin films, and two-dimensional (2D) magnets [8]. On the other hand, MOFE can be used as a time-reversal symmetry-breaking element in optics [11], and its applications such as optical isolators are consequences of time-reversal symmetry breaking [12]. Magnetic materials with large Kerr or Faraday rotation angles have technological applications.

YIG is also known to be MO active [13]. Various experiments have been carried out to study the MOKE and MOFE of iron garnets in the visible and near-UV regime [14,15]. Substituting yttrium with bismuth would result in bismuth iron garnet ($\text{Bi}_3\text{Fe}_5\text{O}_{12}$) (BIG). However, the large radius of bismuth atoms seems to make pure bulk BIG unstable [16]. Thus, pure BIG crystals have not been synthesized [16]. Nonetheless, pure BIG thin films have been grown on suitable garnet substrates, although the lattice constant of the grown

*gyguo@phys.ntu.edu.tw

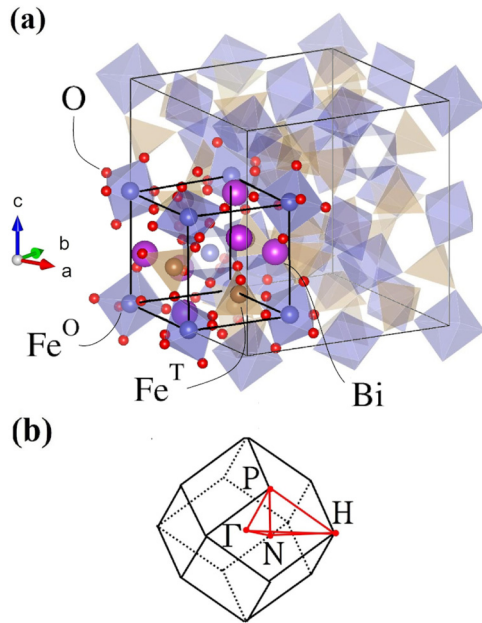


FIG. 1. (a) 1/8 of BIG conventional unit cell. Oxygen atoms are shown as red balls; bismuth atoms are shown as purple balls; Fe^T atoms are shown as yellow balls; Fe^O atoms are shown as blue balls. (b) Brillouin zone of both YIG and BIG. The red lines denote the high symmetry lines where the calculated energy bands will be plotted.

films varies from 12.62–12.67 Å [16]. BIG thin films have approximately seven times larger Faraday rotation angles than that of YIG. The effect of doping bismuth into YIG on the MOFE spectrum was also studied [17,18]. Though numerous experimental studies have been done on these systems, first-principles calculations are scarce. This is probably due to the complexity of the structures of BIG and YIG. As shown in Fig. 1(a), they have a total of 80 atoms in the primitive cell. Although the electronic structures of YIG [19] and BIG [20,21], magnetism, and spin-wave-related properties of YIG [22] have been theoretically studied, no first-principles calculation on the MOKE or MOFE spectra of YIG and BIG have been reported. Therefore, here we carry out a systematic first-principles density functional study on the optical and MO properties of YIG and BIG. The rest of this paper is organized as follows. A brief description of the crystal structures of YIG and BIG as well as the theoretical methods used is given in Sec. II. In Sec. III, the calculated magnetic moments, electronic structure, optical conductivities, MO Kerr, and Faraday effects are presented. Finally, the conclusions drawn from this work are given in Sec. IV.

II. CRYSTAL STRUCTURE AND COMPUTATIONAL METHODS

YIG and BIG crystallize in the cubic structure with space group $Ia\bar{3}d$ [23,24], as illustrated in Fig. 1(a). In each unit cell, there are 48 oxygen atoms at the Wyckoff 96h positions, eight octahedrally coordinated iron atoms (Fe^O) at the 16a positions, and 12 tetrahedrally coordinated iron atoms (Fe^T) at the 24d positions in the primitive cell. In other words, there are two Fe^O ions and three Fe^T ions per formula unit (f.u.).

TABLE I. Structural parameters of $\text{Y}_3\text{Fe}_5\text{O}_{12}$ and $\text{Bi}_3\text{Fe}_5\text{O}_{12}$. For YIG, experimental lattice constant $a = 12.376$ Å and oxygen positions [23] are used. For BIG, experimental lattice constant $a = 12.6469$ Å [24] is used while the oxygen positions are determined theoretically.

$\text{Y}_3\text{Fe}_5\text{O}_{12}$	Wyckoff position	x	y	z
Fe^O	16a	0.0000	0.0000	0.0000
Fe^T	24d	0.3750	0.0000	0.2500
Y	24c	0.1250	0.0000	0.2500
O	96h	0.9726 ^a	0.0572 ^a	0.1492 ^a
$\text{Bi}_3\text{Fe}_5\text{O}_{12}$	Wyckoff position	x	y	z
Fe^O	16a	0.0000	0.0000	0.0000
Fe^T	24d	0.3750	0.0000	0.2500
Bi	24c	0.1250	0.0000	0.2500
O	96h	0.0540	0.0300	0.1485

^aRef. [23].

For YIG, the experimental lattice constant $a = 12.376$ Å, and the experimental Wyckoff parameters for oxygen atoms are $(x, y, z) = (0.9726, 0.0572, 0.1492)$ [23]. We use the experimental lattice constant and atomic positions for all YIG calculations. On the other hand, as mentioned above, BIG crystals have not been synthesized, although stable BIG thin films could be grown on suitable garnet substrates [16]. Furthermore, the atomic positions in BIG films have not been determined experimentally [16]. Therefore, we use the experimental lattice constant for BIG films $a = 12.6469$ Å [24] and determine the atomic positions theoretically (see Table I), as described in the next paragraph. We then use these theoretically determined atomic positions and the experimental lattice constant $a = 12.6469$ Å for all BIG calculations. Nonetheless, we also perform the same calculations for BIG using $a = 12.60$ Å and find that the band structures and optical spectra obtained using these two different lattice constants are nearly identical. Therefore, we believe that the band structure and optical spectra for BIG presented in this paper will not be significantly affected by reasonable variations in the structural parameters of BIG.

Our first-principles calculations are based on the density functional theory with the generalized gradient approximation (GGA) of the Perdew-Burke-Ernzerhof formula [25] to the electron exchange-correlation potential. Furthermore, we use the GGA + U method to have a better description for on-site interaction for Fe d electrons [26]. Here we set $U = 4.0$ eV, which was found to be rather appropriate for iron oxides, in particular, for describing charge-orbital ordering in magnetite (Fe_3O_4) [27] and also for describing exchange interaction and spin wave spectrum in YIG [22]. Indeed, as we will show below, the optical and MO spectra calculated using this U value agree rather well with the available experimental spectra. All the calculations are carried out by using the accurate projector-augmented wave [28] method, as implemented in the Vienna *ab initio* Simulation Package (VASP) [29,30]. The valence electronic configurations of Y, Bi, Fe, and O taken into account are $4s^2 4p^6 5s^2 4d^1$, $6s^2 6p^3$, $3p^6 3d^7 4s^1$, and $2s^2 2p^4$, respectively. A large energy cutoff of 450 eV for the plane-wave basis is used. A $6 \times 6 \times 6$ k -point mesh is used for both

systems in the self-consistent charge density calculations. The convergence criteria for energy is 1.0×10^{-6} eV. For structure relaxation, all atoms are relaxed until residual force is less than $10 \text{ meV}/\text{\AA}$ while the lattice constant is fixed. The density of states (DOS) calculation is performed with a denser k -point mesh of $10 \times 10 \times 10$.

We first calculate the optical conductivity tensor, which determines the MOKE and MOFE. We let the magnetization of our systems be along (001) (z) direction. In this case, our systems have the fourfold rotational symmetry along the z axis and thus the optical conductivity tensor can be written in the following form [31]:

$$\sigma = \begin{pmatrix} \sigma_{xx} & \sigma_{xy} & 0 \\ -\sigma_{xy} & \sigma_{xx} & 0 \\ 0 & 0 & \sigma_{zz} \end{pmatrix}. \quad (1)$$

The optical conductivity tensor can be formulated within the linear response theory. Here the real part of the diagonal elements and imaginary part of the off-diagonal elements are given by [31–33]:

$$\begin{aligned} \sigma_{aa}^1(\omega) &= \frac{\pi e^2}{\hbar\omega m^2} \sum_{i,j} \int_{BZ} \frac{d\mathbf{k}}{(2\pi)^3} |p_{ij}^a|^2 \delta(\epsilon_{\mathbf{k}j} - \epsilon_{\mathbf{k}i} - \hbar\omega), \quad (2) \\ \sigma_{xy}^2(\omega) &= \frac{\pi e^2}{\hbar\omega m^2} \sum_{i,j} \int_{BZ} \frac{d\mathbf{k}}{(2\pi)^3} \text{Im}[p_{ij}^x p_{ji}^y] \delta(\epsilon_{\mathbf{k}j} - \epsilon_{\mathbf{k}i} - \hbar\omega), \quad (3) \end{aligned}$$

where $\hbar\omega$ is the photon energy, and $\epsilon_{\mathbf{k}i(j)}$ are the energy eigenvalues of occupied (unoccupied) states. The transition matrix elements $p_{ij}^a = \langle \mathbf{k}j | \hat{p}_a | \mathbf{k}i \rangle$ where $|\mathbf{k}i(j)\rangle$ are the i th (j th) occupied (unoccupied) states at k point \mathbf{k} , and \hat{p}_a is the Cartesian component a of the momentum operator. The imaginary part of the diagonal elements and the real part of the off-diagonal elements are then obtained from $\sigma_{aa}^1(\omega)$ and $\sigma_{xy}^2(\omega)$, respectively, via the Kramers-Kronig transformations as follows:

$$\sigma_{aa}^2(\omega) = -\frac{2\omega}{\pi} P \int_0^\infty \frac{\sigma_{aa}^1(\omega')}{\omega'^2 - \omega^2} d\omega', \quad (4)$$

$$\sigma_{xy}^1(\omega) = \frac{2}{\pi} P \int_0^\infty \frac{\omega' \sigma_{xy}^2(\omega')}{\omega'^2 - \omega^2} d\omega', \quad (5)$$

where P denotes the principal value of the integration. We can see that Eq. (2) and Eq. (3) neglect transitions across different k points since the momentum of the optical photon is negligibly small compared with the electron crystal momentum and thus only the direct interband transitions need to be considered. In our calculations p_{ij}^a are obtained in the PAW formalism [34]. We use a $10 \times 10 \times 10$ k -point mesh and the Brillouin zone integration is carried out with the linear tetrahedron method (see Ref. [35] and references therein), which leads to well-converged results. To ensure that the $\sigma_{aa}^2(\omega)$ and $\sigma_{xy}^1(\omega)$ in the optical frequency range (e.g., $\hbar\omega < 8$ eV) obtained via Eqs. (4) and (5) are converged, we include the unoccupied states at least 21 eV above the Fermi energy, i.e., a total of 1200 (1300) bands are used in the YIG (BIG) calculations.

For a bulk magnetic material, the complex polar Kerr rotation angle is given by [36,37],

$$\theta_K + i\epsilon_K = \frac{-\sigma_{xy}}{\sigma_{xx}\sqrt{1 + i(4\pi/\omega)\sigma_{xx}}}. \quad (6)$$

Similarly, the complex Faraday rotation angle for a thin film can be written as [38]

$$\theta_F + i\epsilon_F = \frac{\omega d}{2c}(n_+ - n_-), \quad (7)$$

where n_+ and n_- represent the refractive indices for left- and right-handed polarized lights, respectively, and are related to the corresponding dielectric function (or optical conductivity via expressions $n_\pm^2 = \epsilon_\pm = 1 + \frac{4\pi i}{\omega}\sigma_\pm = 1 + \frac{4\pi i}{\omega}(\sigma_{xx} \pm i\sigma_{xy})$). Here the real parts of the optical conductivity σ_\pm can be written as

$$\sigma_\pm^1(\omega) = \frac{\pi e^2}{\hbar\omega m^2} \sum_{i,j} \int_{BZ} \frac{d\mathbf{k}}{(2\pi)^3} |\Pi_{ij}^\pm|^2 \delta(\epsilon_{\mathbf{k}j} - \epsilon_{\mathbf{k}i} - \hbar\omega), \quad (8)$$

where $\Pi_{ij}^\pm = \langle \mathbf{k}j | \frac{1}{\sqrt{2}}(\hat{p}_x \pm i\hat{p}_y) | \mathbf{k}i \rangle$. Clearly, $\sigma_{xy} = \frac{1}{2i}(\sigma_+ - \sigma_-)$, and this shows that σ_{xy} would be nonzero only if σ_+ and σ_- are different. In other words, magnetic circular dichroism is the fundamental cause of the nonzero σ_{xy} and hence the MO effects.

III. RESULTS AND DISCUSSION

A. Magnetic moments

Here we first present calculated total and atom-decomposed magnetic moments in Table I. As expected, $\text{Y}_3\text{Fe}_5\text{O}_{12}$ is a ferrimagnet in which Fe ions of the same type couple ferromagnetically while Fe ions of different types couple antiferromagnetically. Since there are two Fe^O ions and three Fe^T ions in a unit cell, $\text{Y}_3\text{Fe}_5\text{O}_{12}$ is ferrimagnetic with a total magnetic moment per f.u. being $\sim 5.0 \mu_B$ (see Table I). The calculated spin magnetic moments of Fe ions of both types are $\sim 4.0 \mu_B$, being consistent with the high spin state of Fe^{+2} ($d^5 \uparrow t_{2g}^4$) ions in either octahedral or tetrahedral crystal field. We note that the orbital magnetic moments of Fe are parallel to their spin magnetic moments. Nonetheless, the calculated orbital magnetic moments of Fe are small, because of strong crystal field quenching. Interestingly, there is a significant spin magnetic moment on each O ion, and this together with the spin magnetic moment of one net Fe ion per f.u. leads to the total spin magnetic moment per f.u. of $\sim 5.0 \mu_B$. The calculated Fe magnetic moments for both symmetry sites agree rather well with the measured ones of $\sim 4.0 \mu_B$ [39]. The calculated total magnetization of $\sim 5.0 \mu_B/\text{f.u.}$ is also in excellent agreement with the experiment [39].

$\text{Bi}_3\text{Fe}_5\text{O}_{12}$ is also predicted to be ferrimagnetic, although the calculated magnetic moments of both Fe^O and Fe^T ions are slightly smaller than the corresponding ones in $\text{Y}_3\text{Fe}_5\text{O}_{12}$ (see Table I). The total magnetization and local magnetic moments of the other ions in BIG are almost identical to that in YIG. However, the experimental m_{tot} for BIG is only $4.4 \mu_B$ [40], being significantly smaller than the calculated value. As mentioned before, stable high-quality BIG crystals are hard to grow. Consequently, this notable discrepancy in total magnetization between the calculation and the previous experiment

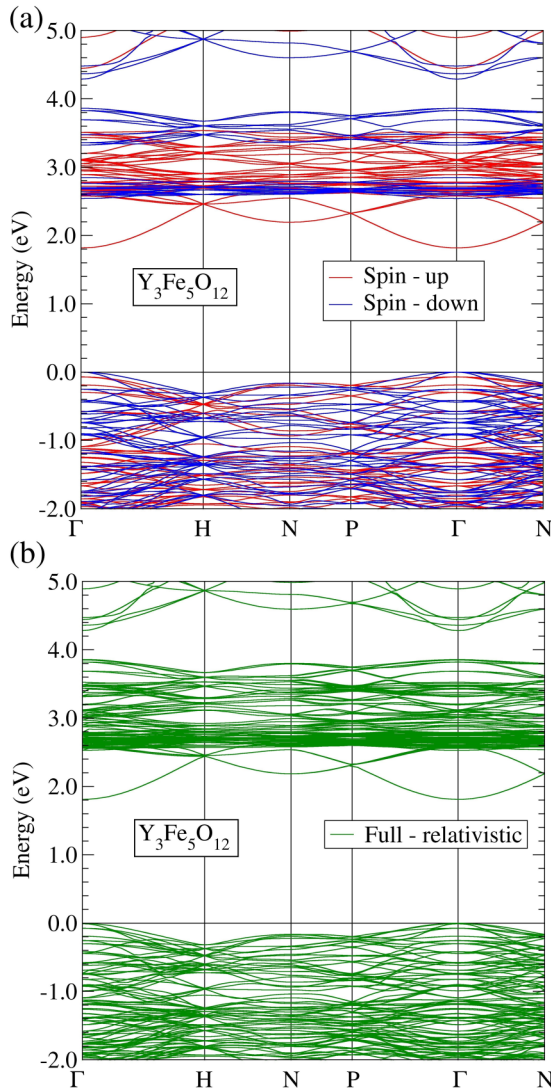


FIG. 2. (a) Scalar-relativistic spin-polarized band structure and (b) fully relativistic band structure of $Y_3Fe_5O_{12}$.

[40] could be due to the poor quality of the samples used in the experiment.

B. Electronic structure

Here we present the calculated scalar-relativistic band structures of YIG and BIG in Fig. 2(a) and Fig. 3(a), respectively. The calculated band structures show that YIG and BIG are both direct band-gap semiconductors, where the conduction band minimum (CBM) and valence band maximum (VBM) are both located at the Γ point. For BIG, both CBM and VBM are purely spin-down bands. This means that BIG is a single-spin semiconductor, which may find applications for spintronic and spin photovoltaic devices. The origin of the MO effects is the magnetic circular dichroism [see Eq. (8)], as mentioned above, which cannot occur without the presence of the spin-orbit coupling (SOC). Therefore, it is useful to examine how the SOC influence the band structures. The fully relativistic band structures for YIG and BIG are presented in Fig. 2(b) and Fig. 3(b), respectively. First, we notice that

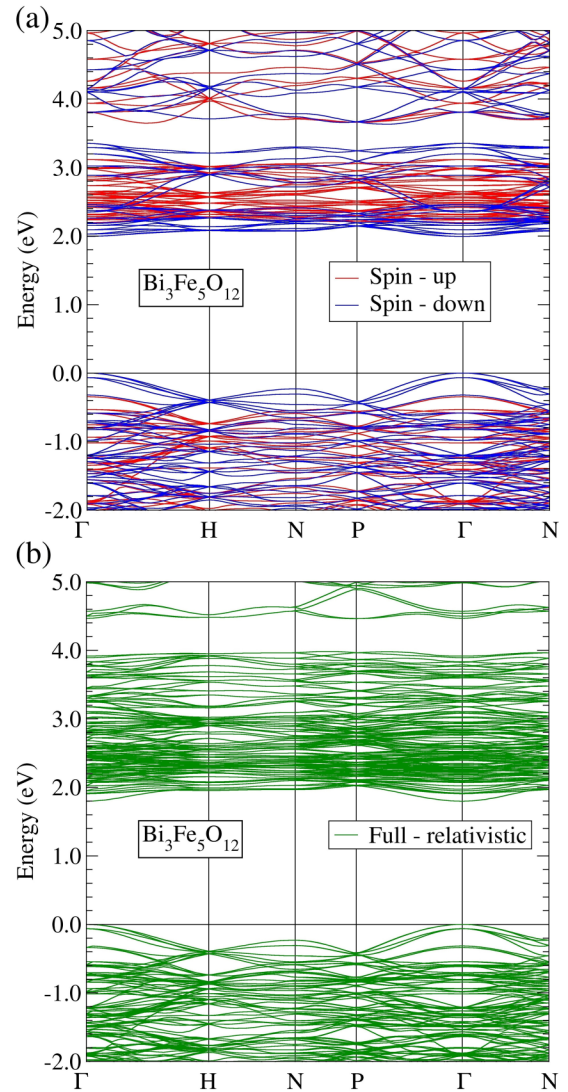


FIG. 3. (a) Scalar-relativistic spin-polarized band structure and (b) fully relativistic band structure of $Bi_3Fe_5O_{12}$.

with the inclusion of the SOC, YIG, and BIG are still direct band-gap semiconductors, where the CBM and VBM are both located at the Γ point. Second, Fig. 3(b) indicates that when the SOC is considered, the BIG band structure changes significantly, while the YIG band structure hardly changes [see Fig. 2(b)]. For example, the band gap for BIG decreases from 2.0 to 1.8 eV after the SOC is included. Also, the gap, which was at 3.4–3.7 eV above the Fermi energy [see Fig. 3(a)], now becomes from 3.9–4.5 eV above the Fermi energy [see Fig. 3(b)]. Interestingly, the substitution of yttrium by bismuth not only enhances the SOC but also changes the electronic band structure significantly, as can be seen by comparing Figs. 2 and 3.

We also calculate total as well as site-, orbital-, and spin-projected densities of states (DOS) for YIG and BIG, as displayed in Figs. 4 and 5, respectively. First, Figs. 4 and 5 show that in both YIG and BIG, the upper valence bands ranging from -4.0 to 0.0 eV, are dominated by O p orbitals with minor contributions from Fe d orbitals as well as Y d orbitals in YIG and Bi sp orbitals in BIG. Second, the lower

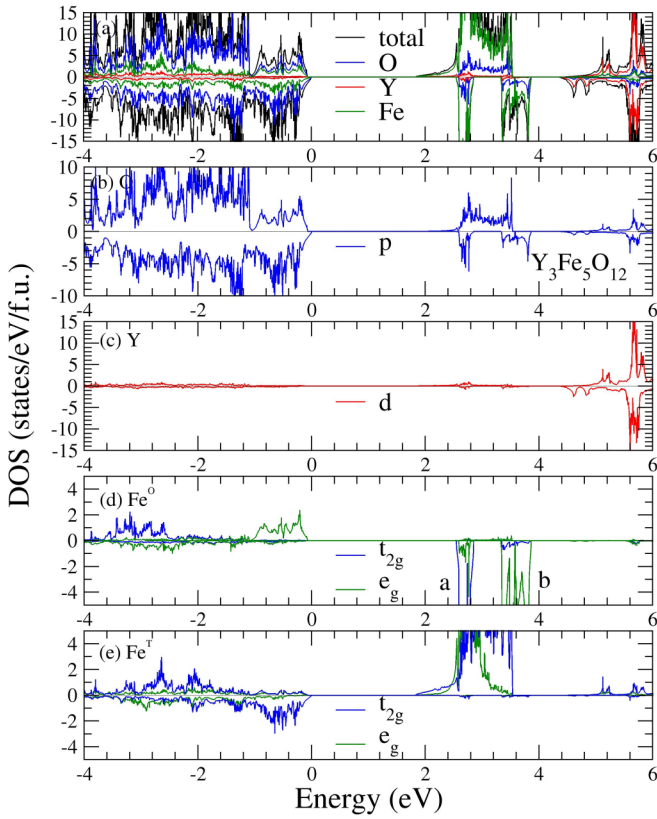


FIG. 4. Spin-polarized density of states (DOS) of $\text{Y}_3\text{Fe}_5\text{O}_{12}$ from the scalar-relativistic calculation.

conduction band manifold, ranging from 1.8 to ~ 3.9 eV in YIG (Fig. 4) and from 2.0–3.4 eV in BIG (Fig. 5), stems predominantly from Fe d orbitals with small contributions from O p orbitals. Therefore, the semiconducting band gaps in YIG and BIG are mainly of the charge transfer type. Furthermore, on the Fe^T sites, the d -DOS in this conduction band is almost fully spin-up [see Figs. 4(e) and 5(e)]. On the Fe^O sites, on the other hand, the d -DOS in this conduction band is almost purely spin-down [see Figs. 4(d) and 5(d)]. Here, the DOS peak marked *a* mostly consists of t_{2g} orbital while that marked *b* above peak *a*, is made up of mainly e_g orbital. The gap between peaks *a* and *b* is thus caused by the crystal field splitting. The above analysis indicates that the d orbitals at the Fe^T sites do not significantly overlap with that at the Fe^O sites since spin-up and spin-down orbitals cannot hybridize with each other. Moreover, the d orbitals of the Fe^T (Fe^O) sites cannot overlap with that of their neighboring Fe^T (Fe^O) sites due to large spatial distances between them. This results in many Fe d -orbital-dominated flat bands in the lower conduction band region, as can be seen in Figs. 2 and 3.

Figure 4 indicates that in YIG, the upper conduction bands from 4.4–6.0 eV are mainly of Y d -orbital character with some contribution from O p orbitals. In BIG, on the other hand, the upper conduction bands from 3.6–6.0 eV are mainly the Bi and O p -orbital hybridized bands (see Fig. 5). Notably, there is sizable Bi sp DOS in the lower conduction band region from 2.0–3.4 eV [see Fig. 5(c)], indicating that the lower conduction bands in BIG are significantly mixed with Bi sp orbitals, as noticed already by Oikawa *et al.* [20]. The

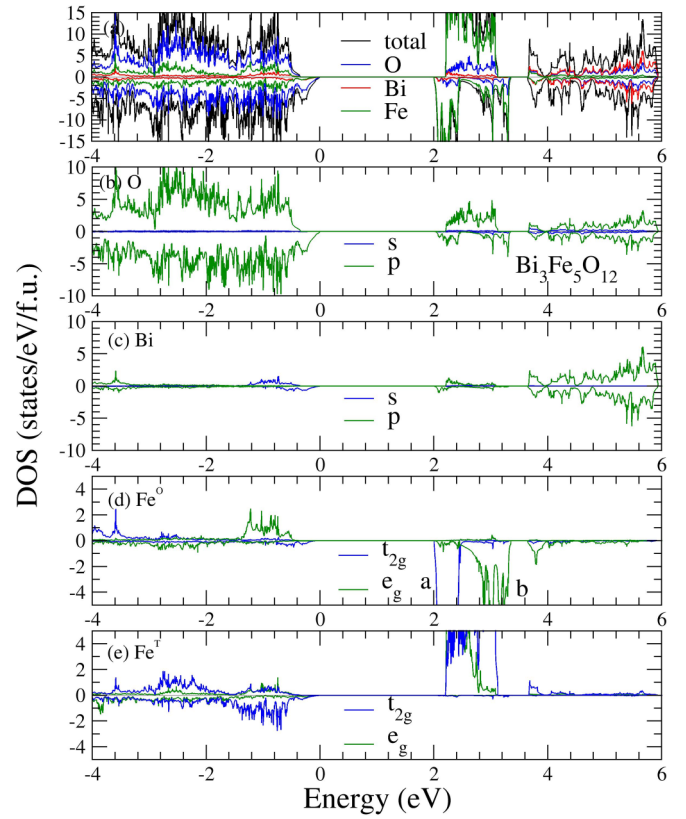


FIG. 5. Spin-polarized density of states (DOS) of $\text{Bi}_3\text{Fe}_5\text{O}_{12}$ from the scalar-relativistic calculation.

Bi p orbital is split into $J = 1/2$ and $J = 3/2$ manifold after SOC is introduced. Since the SOC splitting of the Bi p orbitals is very strong, this explains why the band width of the lower conduction bands in BIG increases from ~ 1.4 to 2.1 eV when the SOC is included (see Fig. 3). In contrast, the band width of the lower conduction bands in YIG remains unaffected by the SOC (see Fig. 2). This also explains why the MO effects in BIG are much stronger than in YIG, as reported in Sec. III.D. below.

C. Optical conductivity

Here we present the optical and magneto-optical conductivities for YIG and BIG, which are ingredients for calculating the Kerr and Faraday rotation angles [see Eq. (6) and Eq. (7)]. In particular, the MO conductivity (i.e., the off-diagonal element of the conductivity tensor σ_{xy}) is crucial, as shown by Eq. (8). Calculated optical conductivity spectra of YIG and BIG are plotted as a function of photon energy in Fig. 6 and Fig. 7, respectively. For YIG, the real part of the diagonal element of the conductivity tensor (σ_{xx}^1) starts to increase rapidly from the absorption edge (~ 2.3 eV) to ~ 4.0 eV, and then further increases with a smaller slope up to ~ 5.6 eV [see Fig. 6(a)]. It then decreases slightly until 6.6 eV and finally increases again with a much steeper slope up to ~ 8.0 eV. Similarly, in BIG, σ_{xx}^1 increases steeply from the absorption edge (~ 2.0 eV) to ~ 4.0 eV, and then further increases with a smaller slope up to ~ 6.0 eV [see Fig. 7(a)]. It then decrease steadily from ~ 6.0 eV to ~ 8.0 eV. The behaviors of

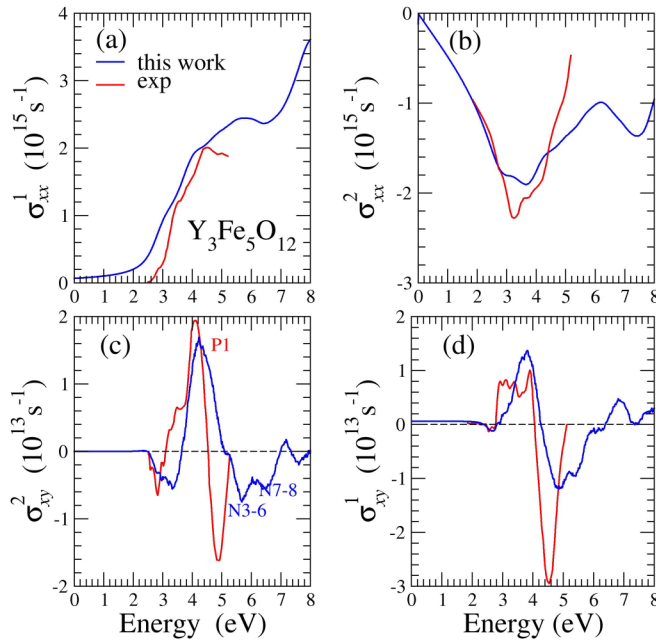


FIG. 6. Calculated optical conductivity of $\text{Y}_3\text{Fe}_5\text{O}_{12}$. (a) Real part and (b) imaginary part of the diagonal element; (c) imaginary part and (d) real part of the off-diagonal element. All the spectra have been convoluted with a Lorentzian of 0.3 eV to simulate the finite quasiparticle lifetime effects. Red lines are the optical conductivity derived from the experimental dielectric constant [14].

the imaginary part of the diagonal element (σ_{xx}^2) of YIG and BIG are rather similar in the energy range up to 5.0 eV [see Figs. 6(b) and 7(b)]. The σ_{xx}^2 spectrum has a broad valley at ~ 3.5 eV (~ 3.0 eV) in the case of YIG (BIG). However, the σ_{xx}^2 spectra of YIG and BIG differ from each other for energy > 5.0 eV. There is a sign change in σ_{xx}^2 occurring at ~ 5.8 eV for BIG, while there is no such a sign change in σ_{xx}^2 of YIG up to 8.0 eV.

The striking difference in the off-diagonal element of the conductivity (σ_{xy}) (i.e., magneto-optical conductivity or magnetic circular dichroism) between YIG and BIG is that σ_{xy} of BIG is almost ten times larger than that of YIG (see Figs. 6 and 7). Nonetheless, the line shapes of the off-diagonal element of YIG and BIG are rather similar except that their signs seem to be opposite and their peaks appear at quite different energy positions. In particular, in the low-energy range up to ~ 4.4 eV, the line shape of the imaginary part of the off-diagonal element (σ_{xy}^2) of BIG looks like an inverted “W” [see Fig. 7(c)], while that of YIG in the energy region up to ~ 7.0 eV seems to have the W shape [see Fig. 6(c)]. The main difference is that the σ_{xy}^2 of BIG decreases oscillatorily from 4.4–8.0 eV. On the other hand, the line shape of the real part of the off-diagonal element (σ_{xy}^1) of BIG looks like an inverted “sine wave” between 2.0 and 4.7 eV [see Fig. 7(d)], while that of YIG appears to be a sine wave between 2.6 and 6.4 eV [see Fig. 6(d)]. The largest magnitude of σ_{xy}^2 of YIG is $\sim 1.7 \times 10^{13} \text{ s}^{-1}$ at ~ 4.2 eV, while that of BIG is $\sim 1.9 \times 10^{14} \text{ s}^{-1}$ at ~ 3.1 eV. The largest magnitude of σ_{xy}^1 of YIG is $\sim 1.4 \times 10^{13} \text{ s}^{-1}$ at ~ 3.8 eV, while that of BIG is $\sim 1.9 \times 10^{14} \text{ s}^{-1}$ at ~ 2.6 eV.

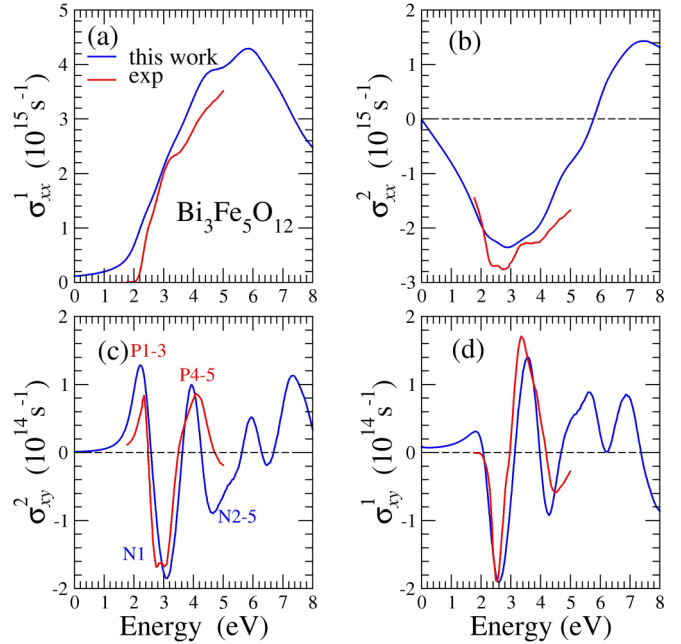


FIG. 7. Calculated optical conductivity of $\text{Bi}_3\text{Fe}_5\text{O}_{12}$. (a) Real part and (b) imaginary part of the diagonal element; (c) imaginary part and (d) real part of the off-diagonal element. All the spectra have been convoluted with a Lorentzian of 0.3 eV to simulate the finite quasiparticle lifetime effects. Red lines are the optical conductivity derived from the experimental dielectric constant [18].

In order to compare with the available experimental data, we also plot the experimental optical conductivity spectra [14,18] in Figs. 6 and 7. The theoretical spectra of the diagonal element of the optical conductivity tensor for both YIG and BIG match well with that of the experimental ones in the measured energy range [see Figs. 6(a) and 6(b) as well as Figs. 7(a) and 7(b)]. Interestingly, we note that the relativistic GGA+ U calculations give rise to the band gaps of YIG and BIG that are smaller than the experimental ones (see Table II), and yet the calculated and measured optical spectra agree rather well with each other. This apparently contradiction can be resolved as follows. In YIG, for example, the lowest conduction bands at $E = 1.8 \sim 2.4$ eV above the VBM are highly dispersive (see Fig. 2) and thus have very low DOS (see Fig. 4). This results in very low optical transition. Therefore, the main absorption edge that appears in the optical spectrum (σ_{xx}^1) is ~ 2.2 eV, which is close to the experimental absorption edge of 2.4 eV, instead of 1.8 eV as determined by the calculated band structure (see Table II). In contrast, no such highly dispersive bands appear at the CBM in BIG. Thus the calculated band gap agrees better with the measured band gap [18] (Table II).

Figures 7(c) and 7(d) show that the calculated σ_{xy}^1 and σ_{xy}^2 of BIG agree almost perfectly with the experimental data [18]. The peak positions, peak heights, and overall trend of the theoretical spectra are nearly identical to that of the experimental ones [18]. On the other hand, the calculated σ_{xy}^1 and σ_{xy}^2 for YIG do not agree so well with the experimental data [14] [Figs. 6(c) and 6(d)]. For example, there is a sharp peak at ~ 4.8 eV in the experimental σ_{xy}^1 spectrum, which seems to

TABLE II. Total spin magnetic moment (m_s^t), atomic spin magnetic moments (m_s^{Fe} , m_s^{O} , m_s^{Bi}), atomic Fe orbital magnetic moments (m_o^{Fe}) and band gap (E_g) of ferrimagnetic $\text{Y}_3\text{Fe}_5\text{O}_{12}$ and $\text{Bi}_3\text{Fe}_5\text{O}_{12}$ from the full-relativistic electronic structure calculations. For comparison, the available measured optical E_g and total magnetization m_{exp}^t are also listed.

structure	m^t (m_{exp}^t) ($\mu_B/\text{f.u.}$)	$m_s^{\text{Fe}(16a)}$ ($m_o^{\text{Fe}(16a)}$) (μ_B/atom)	$m_s^{\text{Fe}(24d)}$ ($m_o^{\text{Fe}(24d)}$) (μ_B/atom)	m_s^{O} (μ_B/atom)	m_s^{Bi} (μ_B/atom)	E_g (E_g^{exp}) (eV)
$\text{Y}_3\text{Fe}_5\text{O}_{12}$	4.999 (5.0 ^a)	-4.177 (-0.016)	4.075 (0.018)	0.067	0.005	1.81 (2.4 ^b)
$\text{Bi}_3\text{Fe}_5\text{O}_{12}$	4.996 (4.4 ^c)	-4.161 (-0.018)	4.068 (0.019)	0.066	0.005	1.82 (2.1 ^d)

^aRef. [39].

^bRef. [14].

^cRef. [40].

^dRef. [18].

be shifted to a higher energy at 5.6 eV with much reduced magnitude in the theoretical σ_{xy}^1 spectrum [see Fig. 6(c)]. Also, for σ_{xy}^2 spectrum, there is a sharp peak at ~ 4.5 eV in the experimental σ_{xy}^2 spectrum, which appears at ~ 4.8 eV with considerably reduced height [see Fig. 6(d)]. Nonetheless, the overall trend of the theoretical σ_{xy} spectra of YIG is in rather good agreement with that of the measured ones [14].

Equations (2), (3), and (8) indicate that the absorptive parts of the optical conductivity elements (σ_{xx}^1 , σ_{zz}^1 , σ_{xy}^2 , and σ_{\pm}^1) are directly related to the dipole allowed interband transitions. Thus, we analyze the origin of the main features in the magneto-optical conductivity (σ_{xy}^2) spectrum by determining the symmetries of the involved band states and the dipole selection rules (see the Appendix for details). The absorptive optical spectra are usually dominated by the interband transitions at the high symmetry points where the energy bands are generally flat (see, e.g., Figs. 2 and 3), thus resulting in large joint density of states. As an example, here we consider the interband optical transitions at the Γ point where the band extrema often occur. Based on the determined band state symmetries and dipole selection rules (see Table III in the Appendix) as well as calculated transition matrix elements [$\text{Im}(p_{ij}^x p_{ji}^y)$], we assign the main features in σ_{xy}^2 [labeled in Figs. 6(c) and 7(c)] to the main interband transitions at the Γ point as shown in Figs. 8 and 9. The details of these assignments, related interband transitions, and transition matrix elements for YIG and BIG are presented in Tables IV and V in the Appendix, respectively. Since there are too many possible transitions to list, we present only those transitions whose transition matrix elements $|\text{Im}(p_{ij}^x p_{ji}^y)| > 0.010$ a.u. in YIG (Table IV) and $|\text{Im}(p_{ij}^x p_{ji}^y)| > 0.012$ a.u. in BIG (Table V).

Figure 8 shows that nearly all the main optical transitions in YIG are from the upper valence bands to the upper conduction bands, and only one main transition (N_3) to the lower conduction bands. Consequently, these transitions contribute

TABLE III. Dipole selection rules for the C_{4h} point group at the Γ point in the Brillouin zone of YIG and BIG.

polarization	Γ_6^+	Γ_5^+	Γ_8^+	Γ_7^+	Γ_6^-	Γ_5^-	Γ_8^-	Γ_7^-
z	Γ_6^-	Γ_5^-	Γ_8^-	Γ_7^-	Γ_6^+	Γ_5^+	Γ_8^+	Γ_7^+
$x + iy$	Γ_5^-	Γ_8^-	Γ_7^-	Γ_6^-	Γ_5^+	Γ_8^+	Γ_7^+	Γ_6^+
$x - iy$	Γ_7^-	Γ_6^-	Γ_5^-	Γ_8^-	Γ_7^+	Γ_6^+	Γ_5^+	Γ_8^+

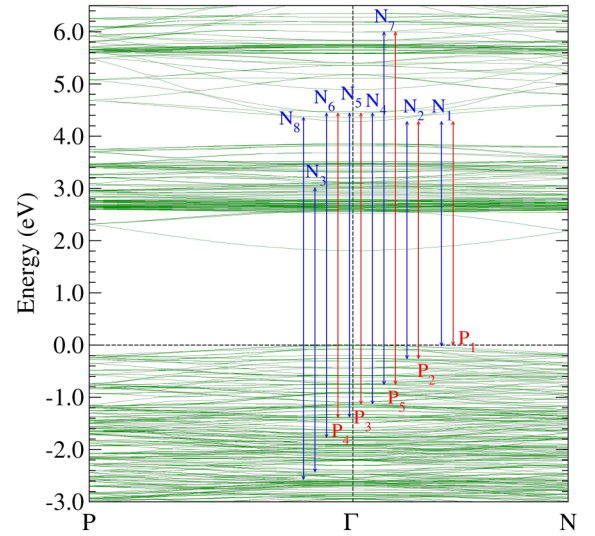


FIG. 8. Relativistic band structures of $\text{Y}_3\text{Fe}_5\text{O}_{12}$. Horizontal dashed lines denote the top of valence band. The principal interband transitions at the Γ point and the corresponding peaks in the σ_{xy} in Fig. 6(c) are indicated by red and blue arrows.

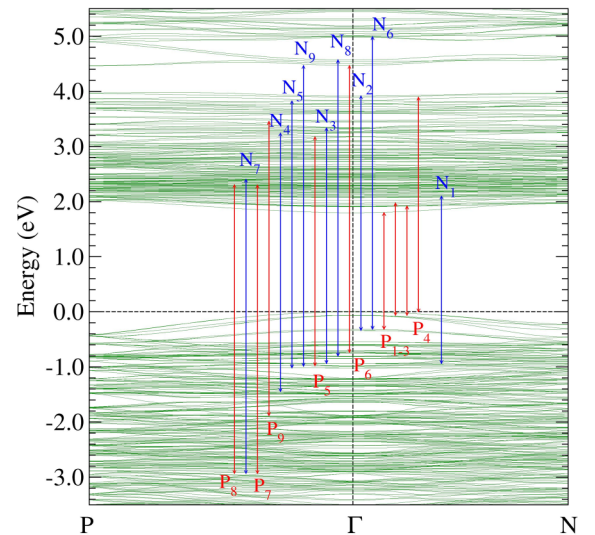


FIG. 9. Relativistic band structures of $\text{Bi}_3\text{Fe}_5\text{O}_{12}$. Horizontal dashed lines denote the top of valence band. The principal interband transitions at the Γ point and the corresponding peaks in the σ_{xy} in Fig. 7(c) are indicated by red and blue arrows.

TABLE IV. Main optical transitions between the states at the Γ point of the Brillouin zone of YIG. Symbols in the first column denote the assigned peaks in the magneto-optical conductivity (σ_{xy}^2) spectrum (Figs. 6 and 8). i and j denote the initial and final states, respectively. $\text{Im}(p_{ij}^x p_{ji}^y)$ denotes the calculated transition matrix element (in atomic units) [see Eq. (3)], and $\sigma_{xy,ij}^2$ denotes the corresponding estimated peak height (in units of 10^{13} Hz) [see Eq. (10)]. E_i and E_j represent the initial and final state energies (in eV), respectively. $\Delta E_{ij} = E_j - E_i$ is the transition energy.

Peak	state i	state j	$\text{Im}(p_{ij}^x p_{ji}^y)$	$\sigma_{xy,ij}^2$	ΔE_{ij}	E_j	E_i
N8	545 (Γ_5^+)	802 (Γ_6^-)	-0.0103	-0.680	6.928	4.358	-2.569
N3	556 (Γ_6^-)	761 (Γ_7^+)	-0.0115	-0.968	5.438	3.010	-2.428
N6	609 (Γ_8^-)	803 (Γ_5^+)	-0.0102	-0.752	6.207	4.442	-1.765
P4	632 (Γ_6^-)	803 (Γ_5^+)	0.0273	2.15	5.825	4.442	-1.384
N5	635 (Γ_8^-)	803 (Γ_5^+)	-0.0251	-1.97	5.818	4.442	-1.376
P3	649 (Γ_6^-)	803 (Γ_5^+)	0.0146	1.20	5.567	4.442	-1.125
N4	651 (Γ_8^-)	803 (Γ_5^+)	-0.0195	-1.61	5.564	4.442	-1.123
N7	668 (Γ_5^+)	844 (Γ_6^-)	-0.0136	-0.926	6.744	5.994	-0.750
P5	670 (Γ_7^+)	844 (Γ_6^-)	0.0119	0.811	6.739	5.994	-0.745
N2	690 (Γ_5^-)	801 (Γ_6^+)	-0.0116	-1.17	4.537	4.280	-0.257
P2	692 (Γ_7^-)	801 (Γ_6^+)	0.0107	1.08	4.535	4.280	-0.254
N1	698 (Γ_5^-)	801 (Γ_6^+)	-0.0431	-4.60	4.292	4.280	-0.012
P1	700 (Γ_7^-)	801 (Γ_6^+)	0.0452	4.84	4.280	4.280	0.000

to the main features in σ_{xy}^2 at photon energy >4.0 eV [see Fig. 6(c)]. In contrast, in BIG, a large number of the main transitions (e.g., N1-5, N7, P1-4, P5-8) are from the upper valence bands to lower conduction bands (see Fig. 9). This gives rise to the main features in σ_{xy}^2 for photon energy <4.0 eV [see Fig. 7(c)], whose magnitudes are generally one order of magnitude larger than that of σ_{xy}^2 in YIG, as mentioned above. The largely enhanced MO activity in BIG stems from the significant hybridization of Bi p orbitals with Fe d orbitals in the lower conduction bands, as mentioned above. Since heavy Bi has a strong spin-orbit coupling, this hybridization

greatly increases the dichroic interband transitions from the upper valence bands to the lower conduction bands in BIG. As mentioned above, Y sd orbitals contribute significantly only to the upper conduction bands in YIG, and this results in the pronounced magneto-optical transitions only from the upper valence bands to the upper conduction bands (Fig. 8). Furthermore, Y is lighter than Bi and thus has a weaker SOC than Bi.

The discussion in the preceding paragraph clearly indicates that the significant hybridization of heavy Bi p orbitals with Fe d orbitals in the lower conduction bands just above the band

TABLE V. Main optical transitions between the states at the Γ point of the Brillouin zone of BIG. Symbols in the first column denote the assigned peaks in the magneto-optical conductivity (σ_{xy}^2) spectrum (Figs. 7 and 9). i and j denote the initial and final states, respectively. $\text{Im}(p_{ij}^x p_{ji}^y)$ denotes the calculated transition matrix element (in atomic units) [see Eq. (3)], and $\sigma_{xy,ij}^2$ denotes the corresponding estimated peak height (in units of 10^{14} Hz) [see Eq. (10)]. E_i and E_j represent the initial and final state energies (in eV), respectively. $\Delta E_{ij} = E_j - E_i$ is the transition energy.

Peak	state i	state j	$\text{Im}(p_{ij}^x p_{ji}^y)$	$\sigma_{xy,ij}^2$	ΔE_{ij}	E_j	E_i
P8	578 (Γ_7^+)	783 (Γ_6^-)	0.0130	0.107	5.234	2.304	-2.930
N7	578 (Γ_7^+)	789 (Γ_8^-)	-0.0123	-0.099	5.331	2.401	-2.930
P7	579 (Γ_5^+)	782 (Γ_8^-)	0.0139	0.114	5.228	2.298	-2.930
P9	661 (Γ_5^-)	856 (Γ_8^+)	0.0136	0.109	5.333	3.452	-1.882
N4	684 (Γ_8^-)	846 (Γ_5^+)	-0.0127	-0.116	4.685	3.242	-1.443
N5	709 (Γ_7^+)	869 (Γ_8^-)	-0.0139	-0.124	4.839	3.825	-1.014
N9	710 (Γ_5^+)	873 (Γ_6^-)	-0.0149	-0.117	5.453	4.467	-0.986
P5	712 (Γ_7^+)	842 (Γ_6^-)	0.0121	0.125	4.153	3.175	-0.979
N3	715 (Γ_8^+)	854 (Γ_5^-)	-0.0135	-0.135	4.271	3.336	-0.935
N8	723 (Γ_8^+)	876 (Γ_5^-)	-0.0142	-0.114	5.374	4.571	-0.803
P6	727 (Γ_7^+)	873 (Γ_6^-)	0.0145	0.120	5.206	4.467	-0.738
N2	741 (Γ_5^-)	872 (Γ_6^+)	-0.0122	-0.123	4.254	3.917	-0.337
N6	743 (Γ_6^-)	878 (Γ_7^+)	-0.0127	-0.103	5.305	4.991	-0.314
P3	743 (Γ_6^-)	749 (Γ_5^+)	0.0184	0.374	2.113	1.799	-0.314
P2	744 (Γ_7^-)	755 (Γ_6^+)	0.0160	0.337	2.037	1.973	-0.063
P1	745 (Γ_8^-)	753 (Γ_7^+)	0.0142	0.308	1.980	1.917	-0.062
P4	747 (Γ_8^-)	871 (Γ_7^+)	0.0138	0.152	3.891	3.891	0.000
N1	715 (Γ_8^+)	760 (Γ_5^-)	-0.0125	-0.177	3.032	2.097	-0.935

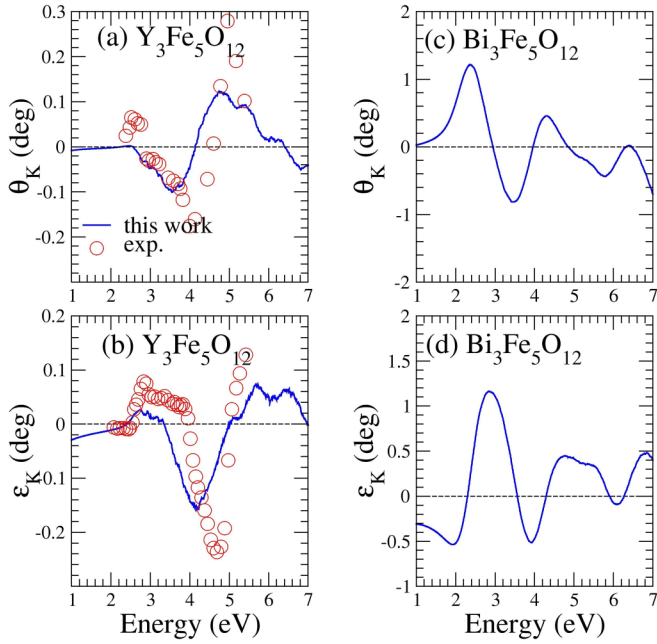


FIG. 10. Calculated complex Kerr rotation angles (blue curves). (a) Kerr rotation (θ_K) and (b) Kerr ellipticity (ϵ_K) spectra of $\text{Y}_3\text{Fe}_5\text{O}_{12}$; (c) Kerr rotation (θ_K) and (d) Kerr ellipticity (ϵ_K) spectra of $\text{Bi}_3\text{Fe}_5\text{O}_{12}$. Red circles in (a) and (b) denote the experimental values from Ref. [15].

gap is the main reason for the large MO effect in BIG [41]. The magnetism in BIG is mainly caused by the iron d orbitals, which have a rather weak SOC. However, through the hybridization between Bi p orbitals and Fe d orbitals, the strong SOC effect is also transferred to the lower conduction bands. Large exchange splitting and strong spin-orbit coupling in the valence and conduction bands below and above the band gap are crucial for strong magnetic circular dichroism and hence large MO effects. Therefore, in search of materials with strong MO effects, one should look for magnetic systems that contain heavy elements such as Bi and Pt [42].

D. Magneto-optical Kerr and Faraday effects

Finally, let us study the polar Kerr and Faraday effects in YIG and BIG. The complex Kerr and Faraday rotation angles for YIG and BIG are plotted as a function of photon energy in Figs. 8 and 9, respectively. First, we notice that the Kerr rotation angles of BIG [Fig. 10(c)] are many times larger than that of YIG [Fig. 10(a)]. For example, the positive Kerr rotation maximum (0.12°) of YIG occurs at ~ 4.8 eV, while that (1.21°) for BIG appears at ~ 2.4 eV. The negative Kerr rotation maximum of -0.10° in YIG occurs at ~ 3.6 eV, while that (-0.80°) for BIG appears at ~ 3.5 eV. This may be expected because Kerr rotation angle is proportional to the MO conductivity (σ_{xy}^1) [Eq. (6)], which in BIG is nearly ten times larger than in YIG, as mentioned in Sec. III C. Similarly, the Kerr ellipticity maximum (0.07°) of YIG occurs at ~ 5.7 eV, whereas that (1.16°) of BIG is located at ~ 2.9 eV. The negative Kerr ellipticity maximum (-0.16°) of YIG occurs at ~ 4.1 eV [Fig. 10(b)] while that (-0.54°) of BIG [Fig. 10(d)] appears at ~ 1.9 eV.

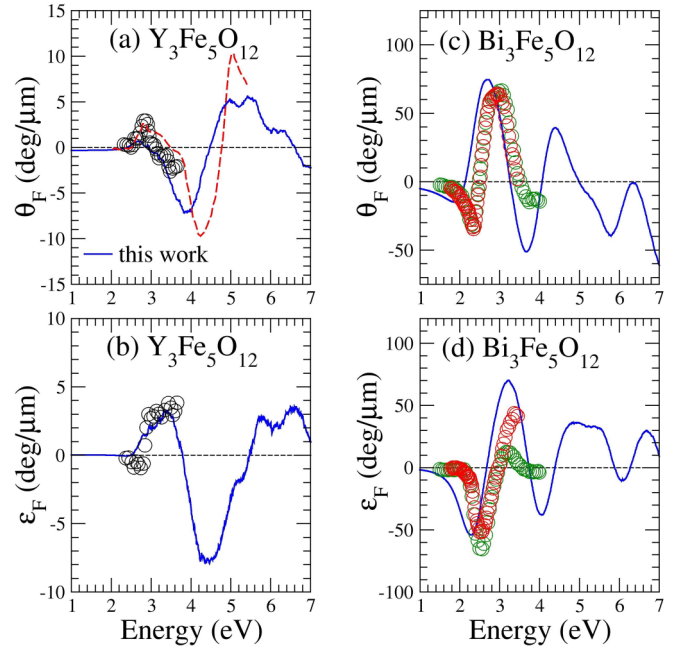


FIG. 11. Calculated complex Faraday rotation angles (blue curves). (a) Faraday rotation (θ_F) and (b) Faraday ellipticity (ϵ_F) spectra of $\text{Y}_3\text{Fe}_5\text{O}_{12}$; (c) Faraday rotation (θ_F) and (d) Faraday ellipticity (ϵ_F) spectra of $\text{Bi}_3\text{Fe}_5\text{O}_{12}$. Red dashed line in (a) denotes the measured values from Ref. [15]. Black circles in (a) and (b) are the experimental values from Ref. [14]. Red (green) circles in (c) and (d) are the experimental values from Ref. [46] ([18]).

Let us now compare our calculated Kerr rotation angles with some known MO materials such as $3d$ transition-metal alloys and compound semiconductors [8]. For magnetic metals, ferromagnetic $3d$ transition metals and their alloys are an important family. Among them, manganese-based pnictides are known to have strong MO effects. In particular, MnBi thin films were reported to have a large Kerr rotation angle of 2.3° [38,43]. Platinum alloys such as FePt, Co_2Pt [42] and PtMnSb [44] also possess large Kerr rotation angles. It was shown that the strong SOC on heavy Pt in these systems is the main cause of the strong MOKE [42]. Among semiconductor MO materials, diluted magnetic semiconductors $\text{Ga}_{1-x}\text{Mn}_x\text{As}$ were reported to show Kerr rotations angle as large as 0.4° at 1.80 eV [45]. Therefore, the strong MOKE effect in YIG and BIG could have promising applications in high-density MO data-storage devices or MO nanosensors with high spatial resolution.

Figure 11 shows that as for the Kerr rotation angles, the Faraday rotation angles of BIG are generally up to ten times larger than that of YIG. The Faraday rotation maximum ($5.7^\circ/\mu\text{m}$) of YIG occurs at ~ 5.4 eV, while that ($74.6^\circ/\mu\text{m}$) for BIG appears at ~ 2.7 eV. The Faraday ellipticity maximum ($3.6^\circ/\mu\text{m}$) of YIG occurs at ~ 6.6 eV, while that ($70.2^\circ/\mu\text{m}$) for BIG is located at ~ 3.2 eV. On the other hand, the negative Faraday rotation maximum ($-7.2^\circ/\mu\text{m}$) of YIG occurs at ~ 3.9 eV, while that ($-51.2^\circ/\mu\text{m}$) of BIG is located at ~ 3.7 eV. The negative Faraday ellipticity maximum ($-7.9^\circ/\mu\text{m}$) for YIG appears at ~ 4.4 eV, whereas that ($-54.1^\circ/\mu\text{m}$) of BIG occurs at ~ 2.3 eV. For comparison, we

notice that MnBi films are known to possess large Faraday rotation angles of $\sim 80^\circ/\mu\text{m}$ at 1.8 eV [38,43].

Finally, we compare our predicted MOKE and MOFE spectra with the available experiments in Figs. 10 and 11. All the predicted MOKE and MOFE spectra are in rather good agreement with the experimental ones in the experimental photon energy range [14,15,18,46]. Nonetheless, our theoretical predictions would have a better agreement with the experiments if all the calculated spectra are blue shifted slightly by ~ 0.3 eV, thus suggesting that the theoretical band gaps are slightly too small.

IV. CONCLUSION

To summarize, we have systematically studied the electronic structure, magnetic, optical, and MO properties of cubic iron garnets YIG and BIG by performing GGA+ U calculations. We find that YIG exhibits significant MO Kerr and Faraday effects in UV frequency range that are comparable to cubic ferromagnetic iron. Strikingly, we find that BIG shows gigantic MO effects in the visible frequency region that are several times larger than YIG. In particular, the Kerr rotation angle of BIG becomes as large as 1.2° at photon energy 2.4 eV, and the Faraday rotation angle for the BIG film reaches $75^\circ/\mu\text{m}$ at 2.7 eV. Calculated MO conductivity (σ_{xy}^2) spectra reveal that these distinctly different MO properties of YIG and BIG result from the fact that the magnitude of σ_{xy}^2 of BIG is nearly ten times larger than that of YIG. Our calculated Kerr and Faraday rotation angles of YIG agree well with the available experimental values. Our calculated Faraday rotation angles of BIG are in nearly perfect agreement with the measured ones. Thus, we hope that our predicted giant MO Kerr effect in BIG will stimulate further MOKE experiments on high-quality BIG crystals.

Principal features in the optical and MO spectra are analyzed in terms of the calculated band structures especially the symmetry of the band states and optical transition matrix elements at the Γ point of the BZ. We find that in YIG, Y sd orbitals mix mainly with the upper conduction bands that are ~ 4.5 eV above the VBM, and thus leave the Fe d orbital dominated lower conduction bands from 1.8–3.8 eV above the VBM almost unaffected by the SOC on the Y atom. In contrast, Bi p orbitals in BIG hybridize significantly with Fe d orbitals in the lower conduction bands and this leads to large SOC-induced band splitting and much increased bandwidth of the lower conduction bands. Consequently, the MO transitions between the upper valence bands and lower conduction bands are greatly enhanced when Y is replaced by heavier Bi. This finding thus provides a guideline in search for materials with desired MO effects, i.e., one should look for magnetic materials with heavy elements such as Bi whose orbitals hybridize significantly with the MO active conduction or valence bands.

Finally, our findings of strong MO effects in these iron garnets and also single-spin semiconductivity in BIG suggest that cubic iron garnets are a useful playground of exploring the interplay of microwave, spin current, magnetism, and optics degrees of freedom, and also have promising applications in high-density semiconductor MO data-storage and low-power consumption spintronic nanodevices.

ACKNOWLEDGMENTS

The authors thank Ming-Chun Jiang for many valuable discussions throughout this work. The authors acknowledge the support from the Ministry of Science and Technology and the National Center for Theoretical Sciences (NCTS) of The R.O.C. The authors are also grateful to the National Center for High-performance Computing (NCHC) for the computing time. G.-Y.G. also thanks the support from the Far Eastern Y. Z. Hsu Science and Technology Memorial Foundation in Taiwan.

APPENDIX: DIPOLE SELECTION RULES AND SYMMETRIES OF BAND STATES AT Γ

In this Appendix, to help identify the origins of the main features in the magneto-optical conductivity $\sigma_{xy}(\omega)$ spectra of YIG and BIG, we provide the dipole selection rules and the symmetries of the band states at the Γ as well as the main optical transitions between them.

Both YIG and BIG have the $Ia\bar{3}d$ space group and thus they have the C_{4h} ($4/m\bar{m}'m'$) point group at the Γ point in the Brillouin zone. Based on the character table of the C_{4h} point group [47], we determine the dipole selection rules for the optical transitions between the band states at the Γ point, as listed in Table III. We calculate the eigenvalues for all symmetry elements of each eigenstate of the Γ point using the IRVSP program [48] and then determine the irreducible representation and hence the symmetry of the state. Based on the obtained symmetries of the band states and also calculated optical matrix elements [$\text{Im}(p_{ij}^x p_{ji}^y)$] [see Eq. (3)], we assign the peaks in the $\sigma_{xy}(\omega)$ spectra of YIG [see Fig. 6(c)] and BIG [see Fig. 7(c)] to the main optical transitions at the Γ point (see Fig. 8 and 9, respectively), as listed in Tables IV and V, respectively.

By integrating the integrand of Eq. (3) over a small sphere near the Γ point, one can estimate the optical spectrum $\sigma_{xy}^2(\omega)$ due to the interband transition from state i to state j ,

$$\sigma_{xy,ij}^2(\omega) = \frac{\pi e^2}{\hbar\omega m^2} \frac{V_{\mathbf{k}}}{(2\pi)^3} \text{Im}[p_{ij}^x p_{ji}^y] L(\epsilon_{\mathbf{k}j} - \epsilon_{\mathbf{k}i} - \hbar\omega), \quad (\text{A1})$$

where the $V_{\mathbf{k}}$ denotes the volume of the small sphere, and the L denotes a Lorentzian of width $\gamma = 0.3$ eV. The radius of the small sphere $V_{\mathbf{k}}$ is taken to be $2\pi/9a$, where a is the lattice constant of YIG or BIG. This is roughly the length scale where the valence bands are flat near the Γ point for YIG and BIG. The estimated peak height is

$$\sigma_{xy,ij}^2 = \frac{\pi e^2}{\hbar\omega m^2} \frac{V_{\mathbf{k}}}{(2\pi)^3} \text{Im}[p_{ij}^x p_{ji}^y] \frac{\hbar}{\pi\gamma}, \quad (\text{A2})$$

and the calculated values are listed in Tables IV and V for YIG and BIG, respectively.

- [1] V. Cherepanov, I. Kolokolov, and V. L'vov, The saga of YIG: spectra, thermodynamics, interaction and relaxation of magnons in a complex magnet, *Phys. Rep.* **229**, 81 (1993).
- [2] S. Mizukami, Y. Ando, and T. Miyazaki, Effect of spin diffusion on Gilbert damping for a very thin permalloy layer in Cu/permalloy/Cu/Pt films, *Phys. Rev. B* **66**, 104413 (2002).
- [3] S. Chikazumi, *Physics of Ferromagnetism*, 2nd ed. (Oxford University Press, Oxford, 1997).
- [4] Y. Kajiwara, K. Harii, S. Takahashi, J. Ohe, K. Uchida, M. Mizuguchi, H. Umezawa, H. Kawai, K. Ando, K. Takanashi, S. Maekawa, and E. Saitoh, Transmission of electrical signals by spin-wave interconversion in a magnetic insulator, *Nature (London)* **464**, 262 (2010).
- [5] T. Schneider, A. A. Serga, B. Leven, B. Hillebrands, R. L. Stamps, and M. P. Kostylev, Realization of spin-wave logic gates, *Appl. Phys. Lett.* **92**, 022505 (2008).
- [6] Y. Sun, H. Chang, M. Kabatek, Y.-Y. Song, Z. Wang, M. Jantz, W. Schneider, M. Wu, E. Montoya, B. Kardasz, B. Heinrich, S. G. E. te Velthuis, H. Schultheiss, and A. Hoffmann, Damping in Yttrium Iron Garnet Nanoscale Films Capped by Platinum, *Phys. Rev. Lett.* **111**, 106601 (2013).
- [7] P. M. Oppeneer, Magneto-optical Kerr Spectra, in *Handbook of Magnetic Materials*, edited by K. H. J. Buschow (Elsevier, Amsterdam, 2001) pp. 229–422.
- [8] V. Antonov, B. Harmon, and A. Yaresko, *Electronic Structure and Magneto-Optical Properties of Solids* (Springer Science & Business Media, Berlin, 2004).
- [9] J. P. Castera, in *Magneto-optical Devices*, Encyclopedia of Applied Physics, edited by G. L. Trigg (Wiley-VCH, New York, 1996), Vol. 9, p. 133.
- [10] M. Mansuripur, *The Principles of Magneto-Optical Recording* (Cambridge University Press, Cambridge, 1995).
- [11] F. D. M. Haldane and S. Raghu, Possible Realization of Directional Optical Waveguides in Photonic Crystals with Broken Time-Reversal Symmetry, *Phys. Rev. Lett.* **100**, 013904 (2008).
- [12] L. J. Aplet and J. W. Carson, A Faraday effect optical isolator, *Appl. Opt.* **3**, 544 (1964).
- [13] J. F. Dillon, Optical properties of several ferrimagnetic garnets, *J. Appl. Phys.* **29**, 539 (1958).
- [14] S. Wittekoek, T. J. A. Popma, J. M. Robertson, P. F. Bongers, Magneto-optic spectra and the dielectric tensor elements of bismuth-substituted iron garnets at photon energies between 2.2–5.2 eV, *Phys. Rev. B* **12**, 2777 (1975).
- [15] F. J. Kahn, P. S. Pershan, and J. P. Remeika, Ultraviolet magneto-optical properties of single-crystal orthoferrites, garnets, and other ferric oxide compounds, *Phys. Rev.* **186**, 891 (1969).
- [16] B. Vertruyen, R. Cloots, J. S. Abell, T. J. Jackson, R. C. da Silva, E. Popova, and N. Keller, Curie temperature, exchange integrals, and magneto-optical properties in off-stoichiometric bismuth iron garnet epitaxial films, *Phys. Rev. B* **78**, 094429 (2008).
- [17] M.-Y. Chern, F.-Y. Lo, D.-R. Liu, K. Yang, and J.-S. Liaw, Red shift of Faraday rotation in thin films of completely bismuth-substituted iron garnet $\text{Bi}_3\text{Fe}_5\text{O}_{12}$, *Jpn. J. App. Phys., Part 1* **38**, 6687 (1999).
- [18] E. Jesenska, T. Yoshida, K. Shinozaki, T. Ishibashi, L. Beran, M. Zahradnik, R. Antos, M. Kučera, and M. Veis, Optical and magneto-optical properties of Bi substituted yttrium iron garnets prepared by metal organic decomposition, *Opt. Mater. Express* **6**, 1986 (2016).
- [19] Y.-N. Xu, Z.-Q. Gu, and W. Y. Ching, First-principles calculation of the electronic structure of yttrium iron garnet ($\text{Y}_3\text{Fe}_5\text{O}_{12}$), *J. Appl. Phys.* **87**, 4867 (2000).
- [20] T. Oikawa, S. Suzuki, and K. Nakao, First-principles study of spin-orbit interactions in bismuth iron garnet, *J. Phys. Soc. Jpn.* **74**, 401 (2005).
- [21] F. Iori, A. Teurtrie, L. Bocher, E. Popova, N. Keller, O. Stéphan, and A. Gloter, Bismut iron garnet: Ab initio study of electronic properties, *Phys. Rev. B* **100**, 245150 (2019).
- [22] L.-S. Xie, G.-X. Jin, L. He, G. E. W. Bauer, J. Barker, and K. Xia, First-principles study of exchange interactions of yttrium iron garnet, *Phys. Rev. B* **95**, 014423 (2017).
- [23] F. Bertaut, F. Forrat, A. Herpin, and P. Mériel, Étude par diffraction de neutrons du grenat ferrimagnétique $\text{Y}_3\text{Fe}_5\text{O}_{12}$, *Compt. rend.* **243**, 898 (1956).
- [24] H. Toraya and T. Okuda, Crystal structure analysis of polycrystalline $\text{Bi}_3\text{Fe}_5\text{O}_{12}$ thin film by using asymmetric and symmetric diffraction techniques, *J. Phys. Chem. Solids* **56**, 1317 (1995).
- [25] J. P. Perdew, K. Burke, and M. Ernzerhof, Generalized Gradient Approximation Made Simple, *Phys. Rev. Lett.* **77**, 3865 (1996).
- [26] S. L. Dudarev, G. A. Botton, S. Y. Savrasov, C. J. Humphreys, and A. P. Sutton, Electron-energy-loss spectra and the structural stability of nickel oxide: An LSDA+ U study, *Phys. Rev. B* **57**, 1505 (1998).
- [27] H.-T. Jeng, G. Y. Guo, and D. J. Huang, Charge-Orbital Ordering and Verwey Transition in Magnetite, *Phys. Rev. Lett.* **93**, 156403 (2004).
- [28] G. Kresse and D. Joubert, From ultrasoft pseudopotentials to the projector augmented-wave method, *Phys. Rev. B* **59**, 1758 (1999).
- [29] G. Kresse and J. Furthmüller, Efficient iterative schemes for *ab initio* total-energy calculations using a plane-wave basis set, *Phys. Rev. B* **54**, 11169 (1996).
- [30] G. Kresse and J. Furthmüller, Efficiency of *ab-initio* total energy calculations for metals and semiconductors using a plane-wave basis set, *Comput. Mat. Sci* **6**, 15 (1996).
- [31] W. Feng, G.-Y. Guo, J. Zhou, Y. Yao, and Q. Niu, Large magneto-optical Kerr effect in noncollinear antiferromagnets Mn_3X ($\text{X} = \text{Rh}, \text{Ir}, \text{Pt}$), *Phys. Rev. B* **92**, 144426 (2015).
- [32] C. S. Wang and J. Callaway, Band structure of nickel: Spin-orbit coupling, the Fermi surface, and the optical conductivity, *Phys. Rev. B* **9**, 4897 (1974).
- [33] P. M. Oppeneer, T. Maurer, J. Sticht, and J. Kübler, *Ab initio* calculated magneto-optical Kerr effect of ferromagnetic metals: Fe and Ni, *Phys. Rev. B* **45**, 10924 (1992).
- [34] B. Adolph, J. Furthmüller, and F. Bechstedt, Optical properties of semiconductors using projector-augmented waves, *Phys. Rev. B* **63**, 125108 (2001).
- [35] W. M. Temmerman, P. A. Sterne, G. Y. Guo, and Z. Szotek, Electronic Structure Calculations of High T_c Materials, *Mol. Simul.* **4**, 153 (1989).
- [36] G.-Y. Guo and H. Ebert, Theoretical investigation of the orientation dependence of the magneto-optical Kerr effect in Co, *Phys. Rev. B* **50**, 10377 (1994).
- [37] G.-Y. Guo and H. Ebert, Band-theoretical investigation of the magneto-optical Kerr effect in Fe and Co multilayers, *Phys. Rev. B* **51**, 12633 (1995).

- [38] P. Ravindran, A. Delin, P. James, B. Johansson, J. Wills, R. Ahuja, and O. Eriksson, Magnetic, optical, and magneto-optical properties of MnX (X=As, Sb, or Bi) from full-potential calculations, *Phys. Rev. B* **59**, 15680 (1999).
- [39] D. Rodic, M. Mitric, R. Tellgren, H. Rundlof, and A. Kremenovic, True magnetic structure of the ferrimagnetic garnet $\text{Y}_3\text{Fe}_5\text{O}_{12}$ and magnetic moments of iron ions, *J. Magn. Magn. Mater.* **191**, 137 (1999).
- [40] N. Adachi, T. Okuda, V. P. Denysenkov, A. Jalali-Roudsar, and A. M. Grishin, Magnetic properties of single crystal film $\text{Bi}_3\text{Fe}_5\text{O}_{12}$ prepared onto $\text{Sm}_3(\text{Sc, Ga})_5\text{O}_{12}(111)$, *J. Magn. Magn. Mater.* **242–245**, 775 (2002).
- [41] P. M. Oppeneer, V. N. Antonov, T. Kraft, and H. Eschrig, First-principles study of the giant magneto-optical Kerr effect in MnBi and related compounds, *J. Appl. Phys.* **80**, 1099 (1996).
- [42] G. Y. Guo and H. Ebert, On the origins of the enhanced magneto-optical Kerr effect in ultrathin Fe and Co multilayers, *J. Magn. Magn. Mater.* **156**, 173 (1996).
- [43] G. Q. Di and S. Uchiyama, Optical and magneto-optical properties of MnBi film, *Phys. Rev. B* **53**, 3327 (1996).
- [44] P. Van Engen, K. Buschow, R. Jongebreur, and M. Erman, PtMnSb, a material with very high magneto-optical kerr effect, *Appl. Phys. Lett.* **42**, 202 (1983).
- [45] R. Lang, A. Winter, H. Pascher, H. Krenn, X. Liu, and J. K. Furdyna, Polar Kerr effect studies of $\text{Ga}_{1-x}\text{Mn}_x\text{As}$ epitaxial films, *Phys. Rev. B* **72**, 024430 (2005).
- [46] M. Deb, E. Popova, A. Fouchet, and N. Keller, Magneto-optical Faraday spectroscopy of completely bismuth-substituted $\text{Bi}_3\text{Fe}_5\text{O}_{12}$ garnet thin films, *J. Phys. D* **45**, 455001 (2012).
- [47] G. F. Koster, J. O. Dimmock, R. G. Wheeler, and H. Statz, *Properties of the Thirty-Two Point Groups*, Vol. 24 (MIT Press, Cambridge, 1963).
- [48] J.-C. Gao, Q.-S. Wu, C. Persson, and Z.-J. Wang, Irvsp: To obtain irreducible representations of electronic states in the VASP, *Comput. Phys. Commun.* **261**, 107760 (2021).